Transport and surface reaction model of a photocatalytic membrane during the radical filtration of methylene blue

Shuyana A. Heredia Deba [a,b], Bas A. Wols [a,c], Doekle R. Yntema [a], Rob G.H. Lammertink [b,*]

[a] Wetsus European Center of Excellence for Sustainable Water Technology, 8911 MA Leeuwarden, The Netherlands
[b] Membrane Science and Technology, Faculty of Science and Technology, University of Twente, Drienerlolaan 5, 7522 NB Enschede, The Netherlands
[c] KWR Watercycle Research Institute, 3430 BB, Nieuwegein, The Netherlands

HIGHLIGHTS

- A photocatalytic membrane was fabricated for water purification and it was tested and described.
- Synergy between photocatalytic degradation and membrane filtration is explored.
- Simple 1D mass transport model describes the dead-end photocatalytic membrane process.
- A methylene blue discoloration of 68–23% was reached with the lowest to the highest filtration rate.

GRAPHICAL ABSTRACT
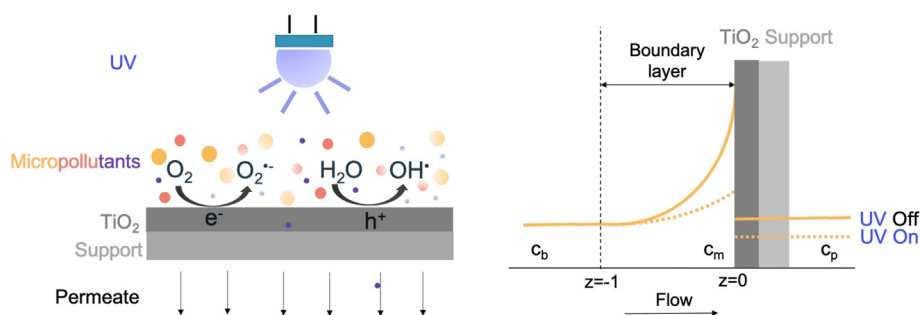
ABSTRACT

This study explores the synergy between photocatalytic oxidation and membrane filtration using a photocatalytic membrane. Titanium dioxide coated alumina membranes were fabricated and tested in a customized Photocatalytic Membrane Reactor (PMR) module. The discoloration of methylene blue (MB), 3.2 mg·L^{-1} in an aqueous solution, was evaluated in dead-end filtration mode. A simple 1D analytic transport and surface reaction model was used based on advection and diffusion, containing intrinsic retention by the membrane and reaction kinetics to predict the permeate concentration. The discoloration of MB by the photocatalytic membrane could be well described by a single retention and reaction rate constant (second Damköhler number) for fluxes from 1.6 to 16.2 L·m^{-2}·h^{-1}. The model furthermore indicates the potential synergy between membrane retention, which leads to increased concentration, and accompanying photocatalytic conversion, at the membrane surface.

© 2022 The Author(s). Published by Elsevier Ltd. This is an open access article under the CC BY license (http://creativecommons.org/licenses/by/4.0/).

1. Introduction

There is a growing need for emerging water contaminants detection, evaluation, and treatment, especially concerning organic micropollutants. Since conventional physicochemical and biological water treatment methods are not prepared for the emerging pollutants, many of these micropollutants could pass through these treatments ending up in the aquatic environment or drinking water (Luo et al., 2014). Advanced oxidation processes (AOPs) and membrane filtration have attracted increasing attention for the protection and remediation of the environment. AOPs produce in situ transitory species (mainly hydroxyl radicals), which degrade toxic and refractory pollutants into water, carbon dioxide, and mineral acids (if the pollutant contains halogens) or at least into more innocuous products (Poyatos et al., 2009).

Among AOPs employing photocatalytic materials, titanium dioxide (TiO₂) has been the most widely studied as it is chemically

---

* Corresponding author.
 E-mail address: r.g.h.lammertink@utwente.nl (R.G.H. Lammertink).

and thermally stable, non-toxic, relatively inexpensive, and commercially available (Fujishima et al., 2000). It all began in 1972 when Fujishima and Honda (1972) observed the photolysis of H_2O in an electrochemical cell composed of TiO_2 and platinum black electrodes. Later, in 1980, Izumi et al. (1980) suggested the reaction mechanism based on photogeneration of hydroxyl radicals. Since then, most investigations have been performed for suspended TiO_2 in laboratory scale since it provides high surface area of catalyst per unit volume, and it has been observed that the rate of reactive oxygen species generation is related to the amount of surface active sites (Nadagouda et al., 2017). Nevertheless, immobilization of photocatalysts prevents the possible release of catalyst nanoparticles to water, sludge generation, and significantly decreases the cost of the treatment by eliminating the photocatalyst recovery step (Ollis, 2003; Rueda-Marquez et al., 2020). Photocatalytic particles have been immobilized on various solid supports including meshes (Grao et al., 2020), monoliths (Konishi et al., 2006), beads (Chiou et al., 2006; Miranda-García et al., 2010), optical fibers (Choi et al., 2001), reactor walls (Dijkstra et al., 2001; Mascolo et al., 2007), spiral glass tubing (Matthews, 1988), and nanotube arrays (Ye et al., 2018). In all immobilized configurations, it is challenging to combine a large surface to volume ratio with significant volumetric production. In microreactors, for example, the surface to volume is large but production flows are typically small (Visan et al., 2014). When immersing a catalytic substrate in a larger volume, the overall conversion is consequently slow (Lin et al., 2012; Murgolo et al., 2015). The chance of contaminants to encounter the catalyst should therefore be increased. One approach to do so, is by advectively forcing the contaminants through the porous catalyst layer such that we do not need to rely on diffusion towards the catalyst.

The configuration thus concerns a photocatalytic membrane reactor (PMR). Membranes have gained an important place in chemical technology and are used in a broad range of applications (Baker, 2012), including separation of TiO_2 particles from purified water and the immobilization of the photocatalyst on their surface. The photocatalytic oxidation synergy with membrane filtration, by degrading and retaining compounds at the membrane surface, has rarely been studied (Tsuru et al., 2001; Aran et al., 2011; Leong et al., 2014). Tsuru et al. (2001) fabricated porous TiO_2 membranes to simultaneously filter and degrade trichloroethylene, while no retention by the membrane was reported, and investigated membrane fouling reduction with polyethyleneimine. Aran et al. (2011) introduced a new porous photocatalytic membrane reactor where the membrane functioned to stabilize the gas-liquid interface to provide O_2 to the reaction zone and enhance the photocatalytic degradation. Leong et al. (2014) reviewed different types of TiO_2 photocatalytic membranes for wastewater treatment and water purification. Consequently, a reactive membrane is expected to reduce the concentration polarization via chemical conversion of reactants, such that higher micropollutants removal rates can be obtained and the production of purified water can be increased. Moreover, the photocatalytic activity can reduce membrane fouling and increase its performance (Nasrollahi et al., 2021).

In the past years, various studies have been carried out to describe the photocatalytic degradation of micropollutants. Ollis already mentioned in his review in 2003 (Ollis, 2003) that more fundamental engineering science models that integrate photocatalytic oxidation and membrane technologies are required. To our knowledge the models created so far consider the membrane as a support (Herz, 2004; Phan et al., 2017) without inclusion of potential retention by the membrane. Herz (2004) described the chemical conversion inside a porous photocatalytic layer while permeating the fluid. The descriptions included different illumination sides, and advective or diffusive transport through the layer. Phan et al. (2017) included both mass transfer correlation and intrinsic reaction kinetics to model the system as a fixed-bed photocatalytic membrane reactor. They confirmed the relevance of the mass transfer rate to the overall conversion.

Our study aims to provide a model that includes the membrane function (rejection) and the photocatalytic oxidation (reaction) by employing dimensionless numbers to relate the transport phenomena and the photocatalytic reaction on the membrane surface, via the Péclet number (Pe) and the second Damköhler number (Da_{II}), respectively. The Da_{II} presents the surface reaction to mass transport rate and therefore is a key parameter for scaling- up (Otálvaro-Marín et al., 2019) as shown previously (Li Puma et al., 2001; Li Puma and Brucato, 2007; Li Puma and Yue, 1998a; Li Puma and Yue, 1998b). In the present study, photocatalytic membranes were fabricated, and their function was experimentally studied in a dead-end configuration. A simple analytic 1D transport and surface reaction model, that successfully describes these experimental results, is provided to elucidate the synergy between photocatalytic oxidation and membrane retention. By generating a fundamental understanding of the underlying processes, transport, and UV radiation distribution and reactivity, this process could be optimized for highly relevant applications.

2. Materials and methods

2.1. Photocatalytic membranes fabrication

α-Alumina (α-Al_2O_3) supports (disc: ø28 mm, 2 mm thick, and 80 nm pore size) were purchased from Pervatech B.V., The Netherlands. A single layer of γ-alumina (γ-Al_2O_3) was deposited on the α-Al_2O_3 discs by dip-coating it in a boehmite sol in a dust-free environment. The α-Al_2O_3 support was brought in contact with boehmite sol for 3 s and subsequently removed from the sol with an angular rate of 0.06 rad·s^{-1}. After calcination at 650 °C in a temperature programmable furnace with air atmosphere during 3 h, an approximately 1.2 μm thick γ-Al_2O_3 layer with an average pore diameter of 5 ± 0.1 nm was obtained. Further details for the fabrication of the γ-alumina coated support can be found elsewhere (Uhlhorn et al., 1998; ten Hove et al., 2017; Abedini et al., 2013). One layer of TiO_2 was formed on the gamma layer following the same dip-coating procedure with 1 % titanium dioxide suspension (Evonik, VP Disp. W 2730 X). The resulted layer was sintered for 2 h at 500 ° C, where the heating and cooling rates were kept at 2 °C·min^{-1}. The cleaning of the membrane after an experiment was carried out following the same thermal treatment since calcination is an effective strategy to clean and regenerate the photocatalyst, allowing its repetitive use (Carp et al., 2004; Miranda-García et al., 2014).

2.2. Membrane characterization

For the characterization of the membrane, high resolution SEM (Analysis Zeiss MERLIN HR-SEM) was used to investigate the morphology and cross-section. The pore size of the membranes was determined by permporometry using cyclohexane as condensing vapor. The experimental procedure is described in detail elsewhere (Cuperus et al., 1992). The phase analysis of the TiO_2 layer was performed by X-ray diffraction (D2 Powder, Bruker) operated with Cu-Kα radiation (λ = 1.54184 Å) in the region 2θ = 20–80°.

Permeability is the flux of a given solvent across a membrane (disc area = 6.2 cm^2) per unit driving force (L·m^{-2}·h^{-1}·bar^{-1}). Water permeability experiments were performed in the same dead-end set-up by measuring the pressure as a function of the flux of liquid. All measurements were conducted in triplicate. The permeability was then calculated as the slope of the flux versus pressure.

2.3. Experimental setup

A schematic of the setup is shown in Fig. 1. The flowrate was controlled by a high pressure syringe pump (NE-8000, WPI) while pressure was measured with a pressure sensor (TK-E-3-E-B02D-X-V, GEFRAN). A poly(methyl methacrylate) (PMMA) photocatalytic membrane reactor (PMR) was custom fabricated with a feed reservoir (10 mm height (L) and ø20 mm) on top of the membrane and a fused silica glass window (FSUVP20-2, Crystran, disc: ø20 mm and 2 mm thick) allowing UV irradiation by a UV-Light Emitting Diode (NCSU276AT). The LED (λ = 365) had an additional lens (AL-12M-119) to narrow the light distribution angle. The LED was connected to a regulated power supply (Delta electronics) and set to a 0.45 A constant current.

The permeate stream was continuously monitored by passing through a flow cell (FIA-Z-SMA-ML-PE flow cell, 10 mm path length) connected to a UV–Vis spectrometer (Flame Model Spectrometer with Sony Detector, Ocean Optics).

2.4. UV light irradiation on the membrane surface

Several configurations were studied to optimize the homogeneity of the light irradiation on the membrane surface, by varying the distance between LED and membrane. The light intensity distribution from the LED was measured with a 3D scanning photometer. This device was built from a 3D printer and equipped with a photo-sensitive detector.

2.5. Photodegradation experiments

To test the TiO$_2$ membranes, dead-end filtration experiments were carried out at ambient temperature with methylene blue solution (MB) (BOOM, CAS 61-73-4), $C_{16}H_{18}ClN_3S$, as an azo dye model compound. An aqueous solution 3.2 mg·L^{-1} of MB dissolved in water containing 1.0 mM sodium sulphate was injected into the setup with flow rates of 1, 2, 4, 6, 8, and 10 mL·h^{-1}, corresponding to fluxes of 1.6, 3.3, 6.5, 9.7, 13.0, and 16.2 L·m^{-2}·h^{-1}, which are in the nanofiltration range. Sodium sulphate anhydrous (VWR chemicals, CAS 7757-82-6), Na$_2$SO$_4$, was used to avoid corrosion in the system. The natural pH of the system was used without further adjustment.

As prior to the experiment, the membranes are equilibrated with the feed solution to ensure the discoloration measurements are caused by the photocatalytic reaction and not by the adsorption on the membrane surface. After equilibrating, when the con-

centration recorded by a UV–Vis spectrometer measured a steady inlet value, the LED was turned on. The pre-adsorption of reactants on the surface of the TiO$_2$ membrane may lead to a more efficient electron transfer process (Matthews, 1988; Tachikawa et al., 2007). The monitored wavelength was 664 nm, corresponding to the maximum absorption peak of MB. The experiment was concluded when the outlet absorbance reached a steady value for each filtration rate. The UV–Vis spectrometer calibration was carried out for different concentrations of MB solutions (from 0.96 to 6.4 mg·L^{-1}).

The input UV radiation was set to 21 mW·cm^{-2}, measured by a power meter (Thorlabs) with a Thermal Power Sensor Head (S310-C). All experiments were carried out in triplicate. Control experiments were carried out with a membrane without the TiO$_2$ layer to rule out effects other than the photocatalytic oxidation in the reaction with MB.

2.6. 1D transport and surface reaction model

Based on 3D CFD evaluations, we observed in our experimental set-up a uniform boundary layer thickness across the membrane surface (see Appendix A). Near the membrane, the velocity assumes a linear profile in the vertical (z) direction. Therefore, assuming a purely perpendicular flow through the membrane with only reaction and retention on the membrane surface, we obtain a steady state advection diffusion balance with a reactive boundary condition. In dimensionless form this is given as:

$$\text{Pe}\frac{dc}{dz} = \frac{d^2c}{dz^2} \qquad (1)$$

With dimensionless distance $z = \tilde{z}/L$, concentration $c = \tilde{c}/c_b$, inlet concentration c_b [mg·L^{-1}] and Péclet number, Pe$= uL/D$, with linear velocity u [m·s^{-1}], liquid reservoir height L [m], and diffusivity D [m^2·s^{-1}]. As boundary conditions, we have a constant inlet concentration at $z = -1$ (for ease of using a positive velocity u).

$$c|_{z=-1} = 1 \qquad (2)$$

The other boundary at $z = 0$ represents the reactive membrane with surface reaction rate constant k' [m·s^{-1}], and intrinsic membrane retention 1-α (with α being the ratio of permeate concentration to concentration at the membrane). Thus, $\alpha = 1$ refers to no retention and $\alpha = 0$ refers to complete retention. The flux continuity through this boundary at $z = 0$ is given as Pe$c - \frac{dc}{dz} - \text{Da}_{II}c = \text{Pe}\alpha c$, equating the advective and diffusive flux towards the membrane and the reaction to the advective outflow (see Appendix B). The reactive
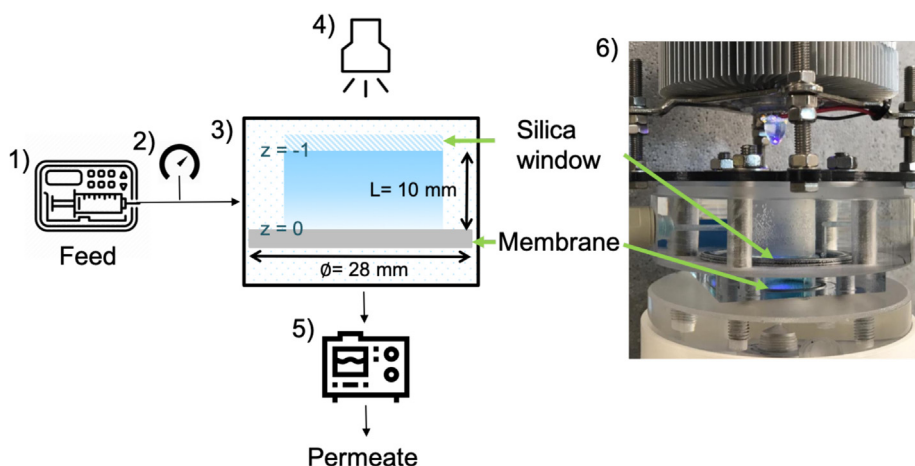

Fig. 1. Experimental setup configuration. Components: (1) syringe pump, (2) pressure indicator, (3) schematic diagram of the PMR, (4) UV lamp, (5) mini spectrometer, and (6) picture of the PMR with the UV lamp.

membrane boundary condition can thus be given as a Robin boundary condition

$$\left.\frac{dc}{dz}\right|_{z=0} = (\mathrm{Pe}(1-\alpha) - \mathrm{Da_{II}})c \tag{3}$$

with the second Damköhler number $\mathrm{Da_{II}} = k'L/D$. This boundary condition includes both the retention by the membrane, through α, as well as the degradation reaction, through $\mathrm{Da_{II}}$. The solution of this ODE with the mentioned boundary conditions reads:

$$c(z) = \frac{e^{(z+1)\mathrm{Pe}}(\mathrm{Pe} - \alpha\mathrm{Pe} - \mathrm{Da_{II}}) + e^{\mathrm{Pe}}(\alpha\mathrm{Pe} + \mathrm{Da_{II}})}{\mathrm{Pe} - \alpha\mathrm{Pe} - \mathrm{Da_{II}} + e^{\mathrm{Pe}}(\alpha\mathrm{Pe} + \mathrm{Da_{II}})} \tag{4}$$

from which we can obtain the concentration at the membrane, which is equal to the concentration polarization as well (as the dimensionless bulk concentration is 1):

$$c(0) = \frac{e^{\mathrm{Pe}}\mathrm{Pe}}{\mathrm{Pe} - \alpha\mathrm{Pe} - \mathrm{Da_{II}} + e^{\mathrm{Pe}}(\alpha\mathrm{Pe} + \mathrm{Da_{II}})} \tag{5}$$

Realize that the outgoing concentration is then equal to $\alpha c(0)$ which corresponds to the concentration in the permeate. By performing experiments where we measure the outlet concentration at different flow rates, so different Pe values, we can fit this equation to obtain information regarding the reaction and retention. In the experiments described here, we will have no retention, so $\alpha = 1$ which simplifies the equation we use for fitting concentration to Pe to:

$$c(0) = \frac{e^{\mathrm{Pe}}\mathrm{Pe}}{e^{\mathrm{Pe}}(\mathrm{Pe} + \mathrm{Da_{II}}) - \mathrm{Da_{II}}} \tag{6}$$

Details of the derivation are found in Appendix B.

3. Results and discussion

3.1. Membrane morphology

Fig. 2 depicts a SEM image of the photocatalytic membrane used for the experiments. The membrane layers are of an average thickness of 1.2 μm for the gamma layer and 3.4 μm for the TiO_2 layer. XRD indicated that the synthesized TiO_2 layer was predominantly composed of anatase (80–90 %) and rutile crystal phases (see Appendix C). The membrane pore size characterization showed

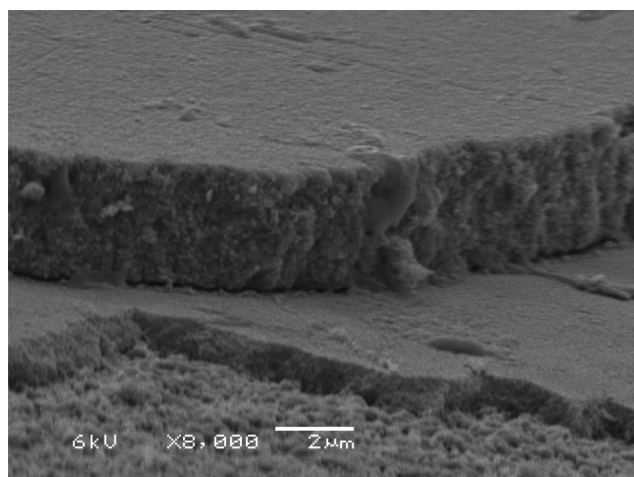5 ± 0.1 nm mesopores, which correspond to the pore size of the γ-alumina layer.

3.2. Pure water permeability

Transmembrane pressure measurements showed that the pressure increases linearly with the pure water flux. Fig. 3 illustrates the pressure measurements under dark conditions and during the experiments with the UV light on. These values were constant over time. The permeability coefficient value for pure water was 4.21 ± 0.02 L·m^{-2}·h^{-1}·bar^{-1} and for MB with the UV light on 4.53 ± 0.02 L·m^{-2}·h^{-1}·bar^{-1} which is typical for nanofiltration membranes. Both permeability values were obtained using the viscosity of water.

The slight increase in permeability suggests that the UV light heats up the solution above the membrane, which reduces its viscosity slightly. Measurements using an infrared camera indeed indicate a temperature increase of about 3 °C. Such a temperature increase is associated with around a 7 % viscosity reduction and it can explain the observed effective permeability change. Following each photocatalytic experiment, the pure water permeability was monitored to confirm the membrane condition.

3.3. Light distribution

The light distribution across the membrane plays an essential role in the photonic efficiency of the system. For a better understanding of the energy distribution, Fig. 4 illustrates the homogeneity of the light intensity for the configuration used during the experiments.

To evaluate the light distribution along the membrane surface, the incident radiation uniformity index was calculated (Appendix D), this index represents how a variable field varies over a surface, where an index value of 1.0 indicates the highest uniformity and it is based on local variations compared to the irradiated area mean value. The average of the scanned values was calculated for the values inside the black circumference. This circle delimits the irradiated membrane area with a diameter of 20 mm, the same as the UV transparent window in the module. An incident radiation uniformity index of 0.86 was obtained, which describes a more uniform light distribution compared to the values obtained in some other studies (Martín-Sómer et al., 2017). As Casado et al. (2017) demonstrated, a higher degree of uniformity can be achieved when smaller areas are used.

Fig. 2. SEM cross-Section (15 degrees tilted) picture of titania and γ-alumina layers on an α-alumina support.
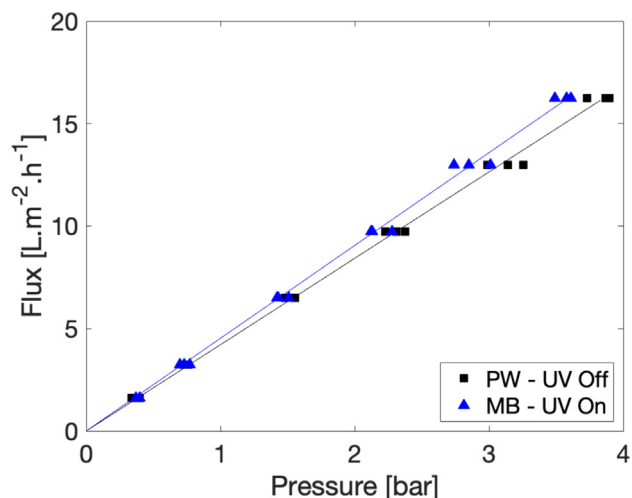

Fig. 3. ■ Pure water flux versus feed pressure and ▲ aqueous methylene blue solution flux versus feed pressure.
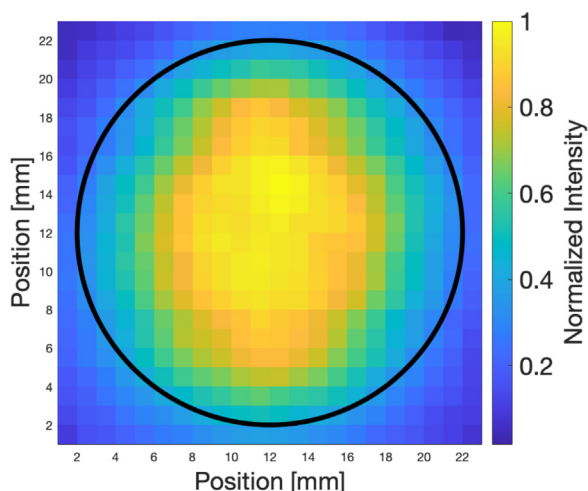
Fig. 4. Normalized incident irradiation over a photocatalytic membrane, represented by the black circumference, located 6 cm from the LED source.

3.4. MB discoloration and transport and surface reaction model

Methylene blue discoloration experiments were conducted in a dead-end PMR under an average irradiation of 21 mW·cm^{-2}. The MB normalized permeate concentration (c_p/c_b) as a function of the Péclet number (Pe) is plotted against the model predictions and shown in Fig. 5. The lines in Fig. 5 represent the mass transport and surface reaction model and the symbols the experimental data. In our case, a value α = 1 was applied as the MB molecules are much smaller (Arias et al., 1999) compared to the membrane pore size, and no retention was observed.

A higher flow rate, greater Pe, resulted in a more concentrated permeate due to the shorter contact time of the pollutant with the photocatalytic surface. An MB discoloration of 68 % was reached at the lowest filtration rate, while only 23 % was achieved for the highest filtration rate.

The experimental data were least squares fitted to the analytical model Eq. 6. A Da$_{II}$ = 18 ± 2 equivalent to a surface reaction constant of 1.0 ± 0.1 ×10^{-6} m·s^{-1} and "bulk" constant of

Fig. 5. Discoloration of MB vs. filtration rate. Symbols depict experimental results and lines correspond to the mass transport and surface reaction model.

$1.6 \pm 0.2 \times10^{-8}$ s^{-1} was obtained. The photocatalytic performance is most commonly quantified in literature by the apparent reaction rate constant, representing the volume based conversion without taking the catalyst area per reactor volume into consideration. A more suitable comparison involves presenting a surface normalized reaction rate constant that represents the catalyst surface reactivity. It is very relevant to note, that in our modeling the surface reaction rate is implemented as a boundary condition, so an infinitely thin reaction zone. Hence, the surface reaction rate constant that we obtain does not reflect the actual catalytic surface that is present inside our thin porous layer, but instead is based on an effective projected surface area *A*. For methylene blue converted by a porous titania layer of similar composition and structure, a surface reaction rate constant of 2.07 ×10^{-7} m·s^{-1} was obtained using an immobilized flow reactor (Visan et al., 2014). As we obtain our surface reaction rate constant by collapsing all conversion inside the porous layer into a boundary condition, we expect the k' we obtain to be larger than the intrinsic surface reaction rate constant. The surface reaction rate constant of a dense titania layer, obtained via reactive sputtering, was measured to be 1.1×10^{-5} m·s^{-1} (Rafieian et al., 2015), but this apparently concerns a different material. Further elucidation of the intrinsic surface reactivity of this photocatalytic membrane involves more detailed modeling that will be covered in ongoing work. For now, our analytic approach does describe the photocatalytic membrane performance reasonably well, which is insightful in understanding the synergy between membrane retention and photocatalytic degradation.

Fig. 6 displays the normalized permeate predictions for different retention factors and second Damköhler number at a constant filtration rate (Pe = 30). Independently of the retention, when there is no reaction (Da$_{II}$ = 0), the steady state outlet concentration for dead-end filtration is the same as the feed (c_p/c_b=1). This results from the concentration polarization (accumulation) at the membrane surface which completely offsets the membrane retention. We also see that for any finite degradation kinetics, the retention enhances the removal. It is clear that within the range of Da$_{II}$ between 1 and 100, some retention will significantly improve the removal. For even more reactive catalysts, the effect of retention becomes less significant.

One needs to realize that this picture is for a given contaminant (here MB). Different compounds have different reactivity towards OH radicals combined with different retention. In practise, this model can help in the optimisation of advanced oxidation processes where these photocatalytic membranes are applied.

4. Conclusion

A porous TiO$_2$ layer onto a γ-Al$_2$O$_3$ layer supported by an α-Al$_2$O$_3$ disc were combined to obtain a photocatalytic membrane. A photocatalytic membrane reactor was designed and fabricated to test the membranes for the UV-driven degradation of methylene blue azo dye model pollutant in water. A 1D transport and surface reaction model that combines membrane retention and photocatalytic oxidation has been provided. This model describes the experimental results obtained for methylene blue discoloration. The development of this model will undoubtedly advance efforts to predict and optimize the use of photocatalytically active membranes for the treatment of (waste) water.

Future work is in progress to test the model with other harmful micropollutants and investigate the UV irradiation and catalytic layer thickness effect.
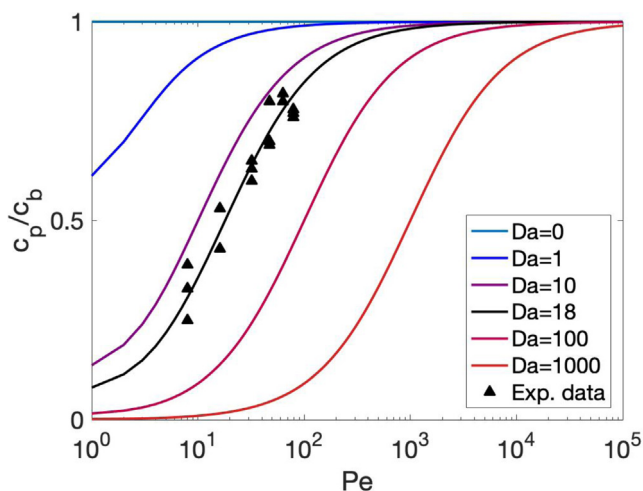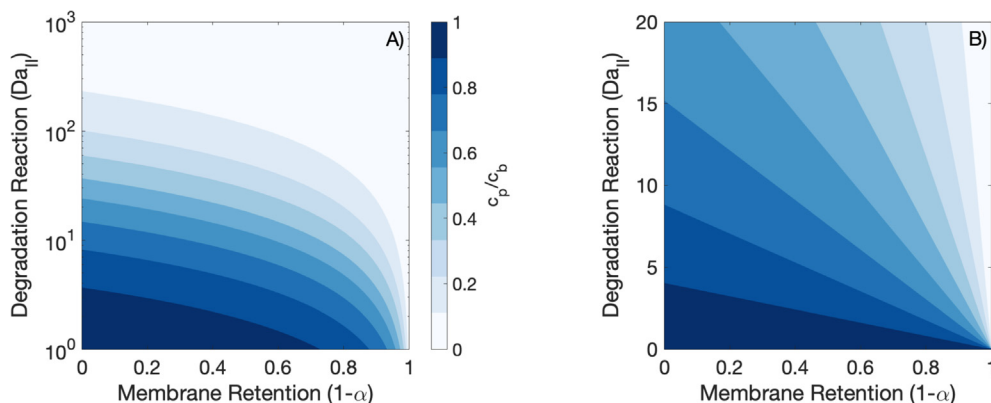
Fig. 6. 1D transport and surface reaction model sensitivity for a filtration rate Pe = 30. Figure A represents a large range of Da_{II} and figure B a close-up of the region with the conditions of the experiments.

Declaration of Competing Interest

The authors declare that they have no known competing financial interests or personal relationships that could have appeared to influence the work reported in this paper.

Acknowledgement

Appendix A. 3D CFD evaluations

Comsol multiphysics 5.6 was used for the CFD modeling. In this model, the module contains a membrane of 0.1 mm thickness and diameter of 20 mm. The water layer on top of the membrane has a thickness of 10 mm (L). The inflow tubing with a diameter of 1 mm and 1 mm height is placed 0.5 mm from the side wall. The water layer below the membrane has a thickness of 0.3 mm. A similar outflow tube as the inflow tube is placed at the centre of the bottom of the module. The mesh consists of 438074 tetrahedral elements. Meshing close to the top and bottom wall and the membrane-water interfaces were done by boundary layers consisting of prism elements (total of 49480 prism elements). Fig. A.7 depicts the 3D view of the module, indicating the cross-section plane.

A laminar flow describes the flow above and through the membrane, a porous media with porosity 0.45 and permeability 2×10^{-18} m² (which corresponds to the measured permeability of the membrane). The walls were treated as no slip boundaries for the flow and no flux for the transport. The inlet velocity was calculated from the feed flows (1 and 10 mL·h^{-1}) for a feed concentration of 1 for the transport.

The applied solver is built-in COMSOL solvers: segregated solver for velocity, pressure, and concentration using Algebraic multigrid solver (that uses a GMRES solver). These are the standard solver settings in Comsol for laminar flow.

The velocity profile across the PMR is shown in Fig. A.8.

To determine the boundary layer thickness, the transport of diluted species is considered. The transport is defined by advection, diffusion, and reaction. For the advection, the velocity field from the laminar flow is used. The diffusion coefficient is set to a value of 5.7×10^{-10} m²·s^{-1} (MB) (Tschirch et al., 2008). In the membrane, a reaction occurs following an exponential decay as in the work from Nielsen et al. (2012): $-kce^{(z/L_{mem})}$, where c is the concentration, k the reaction rate constant, and $\frac{z}{L_{mem}}$ the z-coordinate over the thickness of the membrane (the z coordinate starts at $z = 0$ at the top of the membrane and equals $z = -L_{mem}$ at the bottom. Note this is different from the z-coordinate used in the analytical 1D expression). The value of k is set to 1×10^3 s^{-1}, an arbitrary high value, to ensure a complete reaction in the membrane to see the boundary layer thickness from the diluted species concentration. In the outlet, the conditions were zero pressure and diffusive flux equal to zero.

Fig. A.9 depicts the diluted species concentration for a cross-section in the middle of the cylinder. A uniform boundary layer thickness can be observed for each flow rate which justifies the use of our 1D model.

Appendix B. Derivation of the steady state advection and diffusion balance with a reactive boundary condition

The mass transport of the model compound in the system is determined by the steady state advection and diffusion balance:

$$u\frac{d\tilde{c}}{d\tilde{z}} = D\frac{d^2\tilde{c}}{d\tilde{z}^2} \tag{B.1}$$

with $\tilde{c}$ the concentration, u the permeation velocity, and D the compound's diffusivity. Eq. B.1 is valid for $-L < \tilde{z} < 0$, representing the UV transparent cover and membrane surface, respectively. To make this equation dimensionless, the dimensionless axial coordinate, $z = \tilde{z}/L$, and concentration, $c = \tilde{c}/c_b$ (with inlet concentration c_b), are introduced:

$$\frac{uL}{D}\frac{dc}{dz} = \frac{d^2c}{dz^2} \tag{B.2}$$

where the grouped constants uL/D represent the Péclet number, Pe, thus giving:
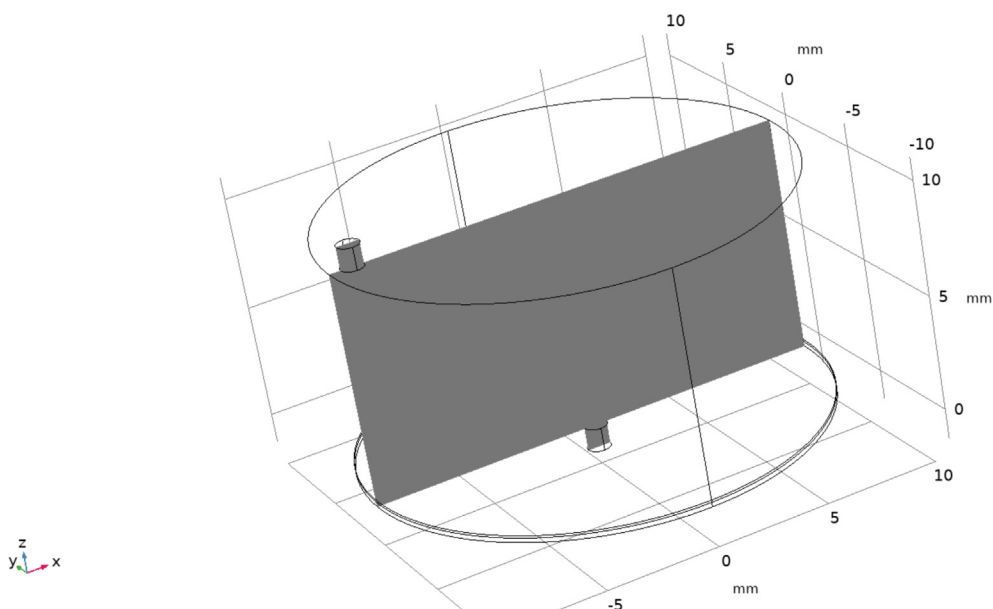
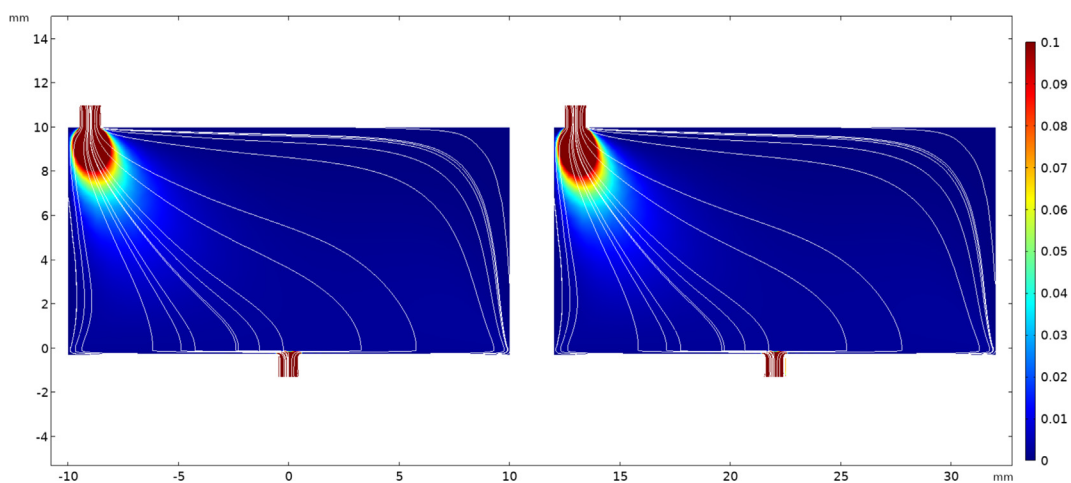**Fig. A.7.** 3D view of the module used for the simulation with the cross-section plane in grey.

Fig. A.8. Cross-sectional view of the velocity profile for an inlet flow of 1 mL·h^{-1} on the left and 10 mL·h^{-1} on the right. The velocity is normalized with the inflow velocity.
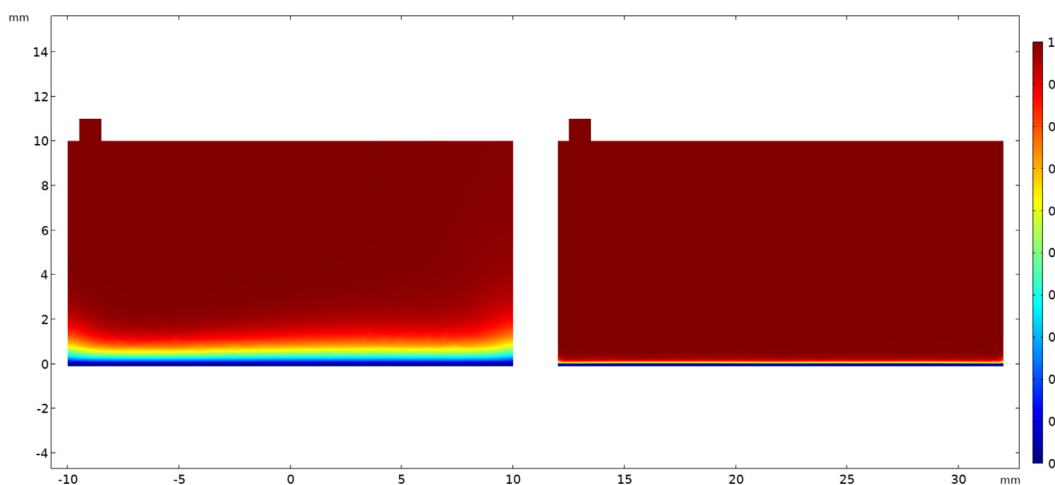

Fig. A.9. Cross-sectional view of the normalized concentration for an inlet flow of 1 mL·h^{-1} on the left and 10 mL·h^{-1} on the right. This figure serves to demonstrate the nearly uniform boundary layer thickness along the membrane surface.

$$\text{Pe}\frac{dc}{dz} = \frac{d^2c}{dz^2} \tag{B.3}$$

Eq. B.3 has the general solution:

$$c(z) = \frac{k_1 e^{\text{Pe}z}}{\text{Pe}} + k_2 \tag{B.4}$$

To solve this equation, two boundary conditions are required. The first one refers to the top cover, located at $z = -1$. The concentration at $z = -1$ is equal to the inlet concentration

$$c(-1) = 1 \tag{B.5}$$

The other boundary, at $z = 0$, represents the reactive membrane with surface reaction rate constant $k\prime$ [m·s^{-1}] and intrinsic membrane retention 1-α (with $\alpha = \tilde{c}_p/\tilde{c}(0)$ being the ratio of permeate concentration to concentration at the membrane). The flux continuity through this boundary at $\tilde{z} = 0$ is given by the advective and diffusive flux towards the membrane balanced by the advective outflow and the surface reaction as:

$$u\tilde{c}(0) - D\frac{d\tilde{c}}{d\tilde{z}}\bigg|_{\tilde{z}=0} = u\tilde{c}_p + k\prime\tilde{c}(0) \tag{B.6}$$

We further know that the intrinsic membrane retention is relating the permeate concentration $\tilde{c}_p$ to the concentration at the membrane $\tilde{c}(0)$ at $\tilde{z} = 0$, by $\tilde{c}_p = \alpha\tilde{c}(0)$. Hence we obtain a description for the concentration gradient at the boundary $\tilde{z} = 0$:

$$\frac{d\tilde{c}}{d\tilde{z}}\bigg|_{\tilde{z}=0} = \frac{1}{D}(u\tilde{c}(0) - u\alpha\tilde{c}(0) - k\prime\tilde{c}(0)) \tag{B.7}$$

which in dimensionless form eventually gives:

$$\frac{dc}{dz}\bigg|_{z=0} = (u - u\alpha - k\prime)c(0)\frac{L}{D} \tag{B.8}$$

The reactive membrane boundary condition can thus be given as a Robin boundary condition

$$\frac{dc}{dz}\bigg|_{z=0} = (\text{Pe}(1-\alpha) - \text{Da}_{\text{II}})c \tag{B.9}$$

with the second Damköhler number $\text{Da}_{\text{II}} = k\prime L/D$ and Péclet number Pe= uL/D. This boundary condition includes both the retention by the membrane, through α, as well as the degradation reaction, through Da_{II}.

Including the first and the second boundary conditions, the following expressions are obtained:

$$c(-1) = \frac{k_1 e^{-\text{Pe}}}{\text{Pe}} + k_2 = 1 \tag{B.10}$$

$$\frac{dc}{dz} = \frac{d}{dz}\left(\frac{k_1 e^{\text{Pe}z}}{\text{Pe}} + k_2\right) = k_1 e^{\text{Pe}z} \tag{B.11}$$

$$\frac{dc}{dz}\bigg|_{z=0} = k_1 = (\text{Pe}(1-\alpha) - \text{Da}_{\text{II}})\left(\frac{k_1}{\text{Pe}} + k_2\right) \tag{B.12}$$

Using Eqs. B.10 and B.12 we can calculate the value of the constants k_1 and k_2:

$$k_2 = \frac{k_1 e^{\text{Pe}z}}{\text{Pe}} - 1 \tag{B.13}$$

$$\frac{k_1}{\frac{k_1}{\text{Pe}} + k_2} = (\text{Pe}(1-\alpha) - \text{Da}_{\text{II}}) \tag{B.14}$$

$$k_1 = \frac{e^{\text{Pe}}\text{Pe}(\text{Pe}(1-\alpha) - \text{Da}_{\text{II}})}{e^{\text{Pe}}\text{Pe} - \text{Pe}(1-\alpha)(e^{\text{Pe}} - 1) + \text{Da}_{\text{II}}(e^{\text{Pe}} - 1)} \tag{B.15}$$

$$k_2 = \frac{\text{Pe}(1-\alpha) - \text{Da}_{\text{II}}}{e^{\text{Pe}}\text{Pe} - \text{Pe}(1-\alpha)(e^{\text{Pe}} - 1) + \text{Da}_{\text{II}}(e^{\text{Pe}} - 1)} \tag{B.16}$$

The general solution, Eq. B.4, including the constants values reads:

$$c(z) = \frac{e^{(z+1)\text{Pe}}(\text{Pe} - \alpha\text{Pe} - \text{Da}_{\text{II}}) + e^{\text{Pe}}(\alpha\text{Pe} + \text{Da}_{\text{II}})}{\text{Pe} - \alpha\text{Pe} - \text{Da}_{\text{II}} + e^{\text{Pe}}(\alpha\text{Pe} + \text{Da}_{\text{II}})} \tag{B.17}$$

In the case where the membrane does not retain the compound, $\alpha = 1$, the equation simplifies to:

$$c(z) = \frac{-\text{Da}_{\text{II}}e^{(z+1)\text{Pe}} + e^{\text{Pe}}(\text{Pe} + \text{Da}_{\text{II}})}{e^{\text{Pe}}(\text{Pe} + \text{Da}_{\text{II}}) - \text{Da}_{\text{II}}} \tag{B.18}$$

which leads to Eq. (6) for $z = 0$.

Appendix C. Membrane crystalline structure

The photocatalytic layer was analysed with XRD. The results show a mixture of anatase and rutile in the TiO$_2$ layer with a strong presence of peaks coming from the alumina support, see Fig. C.10.

The Evonik's suspension (VP Disp. W 2730 X) used for the layer formation has an anatase content of 80–90% by weight with a small portion of rutile. The temperature used for annealing and cleaning is up to 500 °C and the transition temperature to rutile typically occurs between 600 and 700 °C (Nolan et al., 2009), therefore we consider the ratio anatase-rutile in the membrane to be the same as in the dispersion.

Appendix D. Irradiation uniformity index

The light intensity on the photocatalytic membrane surface is expressed in average power density. The uniformity of this distribution is determined using the area weighted uniformity index, γ, given by:

$$\gamma = 1 - \frac{\sum_{i=1}^{n} A_i|\phi_i - \phi_{av}|}{2\phi_{av}\sum_{i=1}^{n} A_i} \tag{D.1}$$

with ϕ_{av} the average light intensity, ϕ_i the local light intensity for pixel i with pixel area A_i. For $\gamma = 1$ we have a uniform intensity distribution.
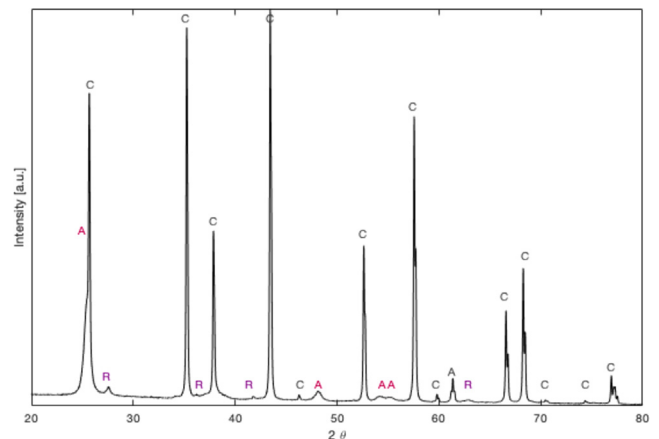

Fig. C.10. X-ray diffraction pattern of the photocatalytic membrane surface: (A) anatase, (R) rutile, and (C) alumina.

References

Abedini, S., Parvin, N., Ashtari, P., Jazi, F.S., 2013. Microstructure, strength and CO_2 separation characteristics of α-alumina supported γ-alumina thin film membrane. Adv. Appl. Ceram. 112 (1), 17–22. https://doi.org/10.1179/1743676112Y.0000000043.

Aran, H., Salamon, D., Rijnaarts, T., Mul, G., Wessling, M., Lammertink, R., 2011. Porous Photocatalytic Membrane Microreactor (P2M2): A new reactor concept for photochemistry. J. Photochem. Photobiol., A 225 (1), 36–41. https://doi.org/10.1016/j.jphotochem.2011.09.022.

Arias, M., López-Periago, J.E., Nuñez Delgado, A., Rubinos, D., Soto, B., Barral, M.T., Dáz-Fierros, F., 1999. Adsorption of Methylene Blue by Red Mud, An Oxide-Rich Byproduct of Bauxite Refining. In: Effect of Mineral-Organic-Microorganism Interactions on Soil and Freshwater Environments. Springer, Boston, MA, pp. 361–365.

Baker, R., 2012. Membrane Technology and Applications. John Wiley & Sons, Ltd., Publication, The Atrium. https://doi.org/10.1016/S0958-2118(96)90133-0.

Carp, O., Huisman, C., Reller, A., 2004. Photoinduced reactivity of titanium dioxide. Prog. Solid State Chem. 32 (1), 33–177. https://doi.org/10.1016/j.progsolidstchem.2004.08.001.

Casado, C., Timmers, R., Sergejevs, A., Clarke, C., Allsopp, D., Bowen, C., van Grieken, R., Marugán, J., 2017. Design and validation of a led-based high intensity photocatalytic reactor for quantifying activity measurements. Chem. Eng. J. 327, 1043–1055. https://doi.org/10.1016/j.cej.2017.06.167.

Chiou, C., Shie, J., Chang, C., Liu, C., Chang, C., 2006. Degradation of di-n-butyl phthalate using photoreactor packed with TiO_2 immobilized on glass beads. J. Hazard. Mater. 137 (2), 1123–1129. https://doi.org/10.1016/j.jhazmat.2006.03.058.

Choi, W., Ko, J.Y., Park, H., Chung, J.S., 2001. Investigation on TiO_2—coated optical fibers for gas—phase photocatalytic oxidation of acetone. Appl. Catal. B Environ. 31 (3), 209–220. https://doi.org/10.1016/S0926-3373(00)00281-2.

Cuperus, F., Bargeman, D., Smolders, C., 1992. Permporometry: the determination of the size distribution of active pores in UF membranes. J. Membr. Sci. 71 (1–2), 57–67. https://doi.org/10.1016/0376-7388(92)85006-5.

Dijkstra, M., Michorius, A., Buwalda, H., Panneman, H., Winkelman, J., Beenackers, A., 2001. Comparison of the efficiency of immobilized and suspended systems in photocatalytic degradation. Catal. Today 66 (2), 487–494. https://doi.org/10.1016/S0920-5861(01)00257-7. catalysis in multiphase reactors.

Fujishima, A., Honda, K., 1972. Performance evaluation and kinetic analysis of photocatalytic membrane reactor in wastewater treatment. Nature 238 (5358), 37–38. https://doi.org/10.1038/238037a0.

Fujishima, A., Rao, T.N., Tryk, D.A., 2000. Titanium dioxide photocatalysis. J. Photochem. Photobiol., C 1 (1), 1–21. https://doi.org/10.1016/S1389-5567(00)00002-2.

Grao, M., Ratova, M., Amorim, C.C., Marcelino, R.B., Kelly, P., 2020. Crystalline TiO_2 supported on stainless steel mesh deposited in a one step process via pulsed dc magnetron sputtering for wastewater treatment applications. J. Mater. Res. Technol. 9 (3), 5761–5773. https://doi.org/10.1016/j.jmrt.2020.03.101.

Herz, R.K., 2004. Intrinsic kinetics of first-order reactions in photocatalytic membranes and layers. Chem. Eng. J. 99 (3), 237–245. https://doi.org/10.1016/j.cej.2003.11.013.

Izumi, I., Dunn, W.W., Wilbourn, K.O., Fan, F.-R.F., Bard, A.J., 1980. Heterogeneous photocatalytic oxidation of hydrocarbons on platinized titanium dioxide powders. J. Phys. Chem. 84 (24), 3207–3210. https://doi.org/10.1021/j100461a015.

Konishi, J., Fujita, K., Nakanishi, K., Hirao, K., 2006. Monolithic TiO_2 with controlled multiscale porosity via a template—free sol—gel process accompanied by phase separation. Chem. Mater. 18 (25), 6069–6074. https://doi.org/10.1021/cm0617485.

Leong, S., Razmjou, A., Wang, K., Hapgood, K., Zhang, X., Wang, H., 2014. TiO_2 based photocatalytic membranes: A review. J. Membr. Sci. 472, 167–184. https://doi.org/10.1016/j.memsci.2014.08.016.

Lin, Y., Tung, K., Tzeng, Y., Chen, J., Chang, K., 2012. Rapid atmospheric plasma spray coating preparation and photocatalytic activity of macroporous titania nanocrystalline membranes. J. Membr. Sci. 309, 83–90. https://doi.org/10.1016/j.memsci.2011.10.018.

Li Puma, G., Brucato, A., 2007. Dimensionless analysis of slurry photocatalytic reactors using two-flux and six-flux radiation absorption-scattering models. Catal. Today 122 (1), 78–90. https://doi.org/10.1016/j.cattod.2007.01.027. materials, Applications and Processes in Photocatalysis.

Li Puma, G., Yue, P.L., 1998a. A laminar falling film slurry photocatalytic reactor. Part I-model development. Chem. Eng. Sci. 53 (16), 2993–3006. https://doi.org/10.1016/S0009-2509(98)00120-1.

Li Puma, G., Yue, P., 1998b. A laminar falling film slurry photocatalytic reactor. Part II-experimental validation of the model. Chem. Eng. Sci. 53 (16), 3007–3021. https://doi.org/10.1016/S0009-2509(98)00119-5.

Li Puma, G., Yue, P., 2001. A novel fountain photocatalytic reactor: model development and experimental validation. Chem. Eng. Sci. 56 (8), 2733–2744. https://doi.org/10.1016/S0009-2509(00)00528-5.

Luo, Y., Guo, W., Ngo, H., Nghiem, L., Hai, F., J.Z., S.L., Wang, X., 2014. A review on the occurrence of micropollutants in the aquatic environment and their fate and removal during wastewater treatment. Sci. Total Environ. 473-474, 619–641. https://doi.org/10.1016/j.scitotenv.2013.12.065.

Martín-Sómer, M., Pablos, C., Grieken, R.V., Marugán, J., 2017. Influence of light distribution on the performance of photocatalytic reactors: LED vs mercury lamps. Appl. Catal. B Environ. 215, 1–7. https://doi.org/10.1016/j.apcatb.2017.05.048.

Mascolo, G., Comparelli, R., Curri, M., Lovecchio, G., Lopez, A., Agostiano, A., 2007. Photocatalytic degradation of methyl red by TiO_2: Comparison of the efficiency of immobilized nanoparticles versus conventional suspended catalyst. J. Hazard. Mater. 142 (1), 130–137. https://doi.org/10.1016/j.jhazmat.2006.07.068.

Matthews, R.W., 1988. Kinetics of photocatalytic oxidation of organic solutes over titanium dioxide. J. Catal. 111 (2), 264–272. https://doi.org/10.1016/0021-9517(88)90085-1.

Miranda-García, N., Maldonado, M.I., Coronado, J., Malato, S., 2010. Degradation study of 15 emerging contaminants at low concentration by immobilized TiO_2 in a pilot plant. Catal. Today 151, 107–113. https://doi.org/10.1016/j.cattod.2010.02.044.

Miranda-García, N., Suárez, S., Maldonado, M.I., Malato, S., Sánchez, B., 2014. Regeneration approaches for TiO_2 immobilized photocatalyst used in the elimination of emerging contaminants in water. Catal. Today 230, 27–34. https://doi.org/10.1016/j.cattod.2013.12.048 (selected contributions of the 4th International Conference on Semiconductor Photochemistry (SP4)).

Murgolo, S., Petronella, F., Ciannarella, R., Comparelli, R., Agostiano, A., Curri, M., Mascolo, G., 2015. UV and solar-based photocatalytic degradation of organic pollutants by nano-sized TiO_2 grown on carbon nanotubes. Catal. Today 240, 114–124. https://doi.org/10.1016/j.cattod.2014.04.021.

Nadagouda, M., Han, C., Pillai, S., McGuinness, N., Byrne, C., Falaras, P., Kontos, A., Gracia-Pinilla, M., Mangalaraja, R., O'Shea, K., Dionysiou, D., 2017. Chapter 8 - Photocatalysis as an Effective Advanced Oxidation Process. In: Stefan, M.I. (Ed.), Advanced Oxidation Processes for Water Treatment: Fundamentals & Applications. IWA Publishing, London, UK, p. 333.

Nasrollahi, N., Ghalamchi, L., Vatanpour, V., Khataee, A., 2021. Photocatalytic-membrane technology: a critical review for membrane fouling mitigation. J. Ind. Eng. Chem. 93, 101–116. https://doi.org/10.1016/j.jiec.2020.09.031.

Nielsen, M.G., In, S.I., Vesborg, P.C., Pedersen, T., Almtoft, K.P., Andersen, I.H., Hansen, O., Chorkendorff, I., 2012. A generic model for photocatalytic activity as a function of catalyst thickness. J. Catal. 289, 62–72. https://doi.org/10.1016/j.jcat.2012.01.015.

Nolan, N.T., Seery, M.K., Pillai, S.C., 2009. Spectroscopic investigation of the anatase-to-rutile transformation of sol-gel-synthesized TiO_2 photocatalysts. J. Phys. Chem. C 113 (36), 16151–16157. https://doi.org/10.1021/jp904358g.

Ollis, D.F., 2003. Integrating Photocatalysis and Membrane Technologies for Water Treatment. Ann. N. Y. Acad. Sci. 984 (1), 65–84. https://doi.org/10.1111/j.1749-6632.2003.tb05993.x.

Otálvaro-Marín, H.L., González-Caicedo, F., Arce-Sarria, A., Mueses, M.A., Crittenden, J.C., Machuca-Martinez, F., 2019. Scaling-up a heterogeneous H_2O_2/TiO_2/solar-radiation system using the Damköhler number. Chem. Eng. J. 364 (January), 244–256. https://doi.org/10.1016/j.cej.2019.01.141.

Phan, D.D., Babick, F., Nguyen, M.T., Wessely, B., Stintz, M., 2017. Modelling the influence of mass transfer on fixed-bed photocatalytic membrane reactors. Chem. Eng. Sci. 173, 242–252. https://doi.org/10.1016/j.ces.2017.07.043.

Poyatos, J.M., Muñio, M.M., Almecija, M.C., Torres, J.C., Hontoria, E., Osorio, F., 2009. Advanced oxidation processes for wastewater treatment: State of the art. Water Air Soil Pollut. 205 (1), 187. https://doi.org/10.1007/s11270-009-0065-1.

Rafeian, D., Driessen, R.T., Ogieglo, W., Lammertink, R.G.H., 2015. Intrinsic photocatalytic assessment of reactively sputtered TiO_2 films. ACS Appl. Mate. Interfaces 7 (16), 8727–8732. https://doi.org/10.1021/acsami.5b01047.

Rueda-Marquez, J., Levchuk, I., Fernández Ibañez, P., Sillanpää, M., 2020. A critical review on application of photocatalysis for toxicity reduction of real wastewaters. J. Cleaner Prod. 258, 120694. https://doi.org/10.1016/j.jclepro.2020.120694.

Tachikawa, T., Fujitsuka, M., Majima, T., 2007. Mechanistic Insight into the TiO_2 Photocatalytic Reactions: Design of New Photocatalysts. J. Phys. Chem. C 111 (14), 5259–5275. https://doi.org/10.1021/jp069005u.

ten Hove, M., Luiten-Olieman, M.W., Huiskes, C., Nijmeijer, A., Winnubst, L., 2017. Hydrothermal stability of silica, hybrid silica and zr-doped hybrid silica membranes. Sep. Purif. Technol. 189, 48–53. https://doi.org/10.1016/j.seppur.2017.07.045.

Tschirch, J., Dillert, R., Bahnemann, D., Proft, B., Biedermann, A., Goer, B., 2008. Photodegradation of methylene blue in water, a standard method to determine the activity of photocatalytic coatings? Res. Chem. Intermed. 34 (4), 381–392. https://doi.org/10.1163/156856708784040588.

Tsuru, T., Toyosada, T., Yoshioka, T., Asaeda, M., 2001. Photocatalytic reactions in a filtration system through porous titanium dioxide membranes. J. Chem. Eng. Jpn. 34 (6), 844–847. https://doi.org/10.1252/jcej.34.844.

Uhlhorn, R.J.R., Huis In't Veld, M.H.B.J., Keizer, K., Burggraaf, A.J., 1998. Synthesis of ceramic membranes. J. Mater. Sci. 27(2), 527–537. https://doi.org/10.1007/BF00543947.

Visan, A., Rafeian, D., Ogieglo, W., Lammertink, R.G.H., 2014. Modeling intrinsic kinetics in immobilized photocatalytic microreactors. Appl. Catal. B: Environ. 150–151, 93–100. https://doi.org/10.1016/j.apcatb.2013.12.003.

Ye, Y., Feng, Y., Bruning, H., Yntema, D., Rijnaarts, H., 2018. Photocatalytic degradation of metoprolol by TiO_2 nanotube arrays and UV-LED: Effects of catalyst properties, operational parameters, commonly present water constituents, and photo-induced reactive species. Appl. Catal. B: Environ. 220, 171–181. https://doi.org/10.1016/j.apcatb.2017.08.040.